Density functional theory study of bulk and single-layer magnetic semiconductor $CrPS_4$

Houlong L. Zhuang[1,*] and Jia Zhou[2,†]

[1]*Department of Mechanical and Aerospace Engineering, Princeton University, Princeton, New Jersey 08544, USA*

[2]*MIIT Key Laboratory of Critical Materials Technology for New Energy Coversion and Storage, School of Chemistry and Chemical Engineering, Harbin Institute of Technology, Harbin 1500001, China*

(Received 9 September 2016; published 16 November 2016)

Searching for two-dimensional (2D) materials with multifunctionality is one of the main goals of current research in 2D materials. Magnetism and semiconducting are certainly two desirable functional properties for a single 2D material. In line with this goal, here we report a density functional theory (DFT) study of bulk and single-layer magnetic semiconductor $CrPS_4$. We find that the ground-state magnetic structure of bulk $CrPS_4$ exhibits the A-type antiferromagnetic ordering, which transforms to ferromagnetic (FM) ordering in single-layer $CrPS_4$. The calculated formation energy and phonon spectrum confirm the stability of single-layer $CrPS_4$. The band gaps of FM single-layer $CrPS_4$ calculated with a hybrid density functional are within the visible-light range. We also study the effects of FM ordering on the optical absorption spectra and band alignments for water splitting, indicating that single-layer $CrPS_4$ could be a potential photocatalyst. Our work opens up ample opportunities of energy-related applications of single-layer $CrPS_4$.

DOI: 10.1103/PhysRevB.94.195307

I. INTRODUCTION

Magnetic semiconductors are an important category of materials that exhibit magnetism in combination with semiconducting properties [1]. Typical examples of magnetic semiconductors include transition-metal oxides (e.g., NiO) [2,3] and chalcogenides (e.g., $FeCr_2S_4$) [4]. Among many known magnetic semiconductors, the ones that possess layered structures (e.g., $CrXTe_3$; X = Si, Ge, and Sn) [5–9] with a van der Waals (vdW) gap between the layers are of particular interest, as they could be thinned down to a single layer, which is often associated with improved properties due to the dimension reduction.

A number of single-layer magnetic semiconductors have been predicted via Kohn-Sham density functional theory (DFT) simulations [10–13]. Most of the proposed applications of the magnetic semiconductors center around employing the spin degree of freedom for spintronics devices [6]. By contrast, significantly fewer studies have explored solar-energy-related applications of single-layer magnetic semiconductors. To fill this gap, Zhang *et al.* recently computed the band-edge positions of single-layer antiferromagnetic (AFM) $MnPSe_3$ and suggested this single-layer material could be a promising photocatalyst for water splitting [14].

Inspired by three previous experimental reports [15–17], here we focus on a relatively less well known magnetic semiconductor $CrPS_4$. Diehl and Carpentier [15] first synthesized bulk $CrPS_4$ and determined its layered structure. Louisy *et al.* measured the magnetic susceptibility and optical spectra of bulk $CrPS_4$ [16]. More recently, Pei *et al.* studied spin dynamics, electronic, and thermal transport properties of bulk $CrPS_4$ [17]. In spite of these experimental studies of bulk $CrPS_4$, theoretical perspectives on this compound are still lacking. Furthermore, although two of the experiments [16,17] have shown bulk $CrPS_4$ is AFM, no direct evidence exists to clarify a specific type of AFM ordering.

In this work, we perform DFT calculations on bulk $CrPS_4$ with the ferromagnetic (FM) and four different types of AFM ordering. We find that the A-type AFM structure is the ground state, albeit the total energy of the FM structure is nearly degenerate. We further predict that single-layer $CrPS_4$ remains semiconducting, while the magnetic structure becomes FM. We show that the formation energy of single-layer $CrPS_4$ is sufficiently small, so that it could be obtained from mechanically exfoliating bulk $CrPS_4$. The computed phonon spectrum of single-layer $CrPS_4$ confirms the dynamical stability. The band gaps of FM single-layer $CrPS_4$ are not only wider than those of bulk $CrPS_4$ but also within the range of visible light, which is promising for solar-energy-conversion applications. Finally, we demonstrate an example of these applications by showing that the band-edge positions of single-layer $CrPS_4$ are energetically favorable for splitting water to generate hydrogen.

II. METHODS

We perform spin-polarized DFT simulations on bulk and single-layer $CrPS_4$ using the Vienna Ab initio Simulation Package (VASP) [18,19]. We employ the Perdew-Burke-Ernzerhof (PBE) [20] functional to describe the exchange and correlation. We also use the van der Waals density functional with optimized Becke88 parameterizations (vdW-DF-optB88) [21–24] functional to account for the interlayer van der Waals interactions in bulk $CrPS_4$. We employ the PBE version of the projector augmented-wave (PAW) [25,26] potentials with the $3s^2 3p^6 3d^5 4s^1$ states of Cr, the $3s^2 3p^3$ states of P, and the $3s^2 3p^4$ states of S treated as valence electrons. The truncated plane-wave basis set has a cutoff energy of 500 eV. As the initial input geometry for the subsequent optimizations, the bulk $CrPS_4$ structure documented in the Inorganic Crystal Structure Database (ICSD) [27] with the ID number 626520 is used. We use one layer of the bulk structure to build a supercell model for single-layer $CrPS_4$ with a vacuum spacing of 18 Å, which is sufficiently large to separate the image interactions

*hzhuang@princeton.edu

†jiazhou@hit.edu.cn

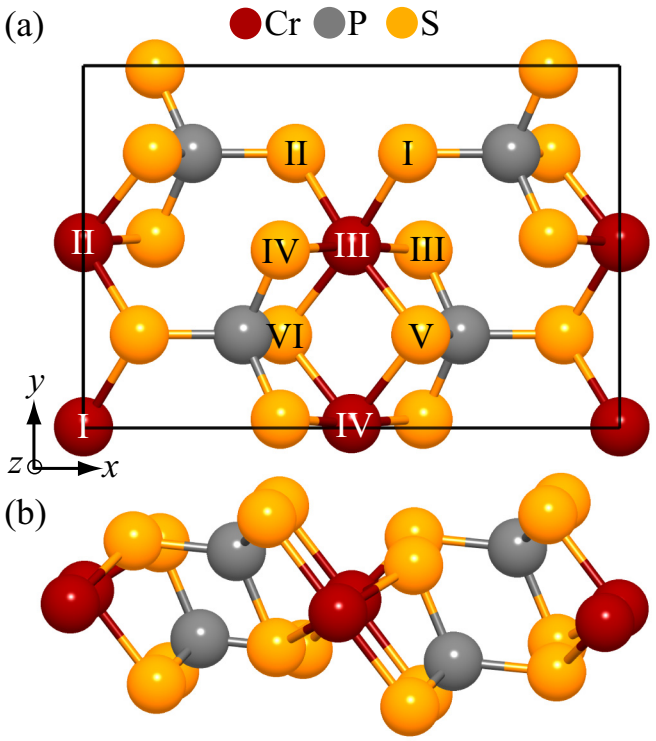

FIG. 1. Schematic illustration of (a) top and (b) side views of a unit cell of single-layer $CrPS_4$.

between the layers. Figure 1 illustrates a single-layer $CrPS_4$ unit cell. The four Cr atoms in the unit cell on the xy plane form a trapezoidlike configuration. Each Cr atom locates at the center of a distorted octahedron with six neighboring S atoms. Viewed along the y direction, the crystal structure of single-layer $CrPS_4$ is a quasi-one-dimensional structure with chains of distorted CrS_6 octahedra bridged by P atoms. Integration over the first Brillouin zone is carried out on $6 \times 9 \times 1$, $6 \times 9 \times 12$, $6 \times 9 \times 12$, and $6 \times 9 \times 6$ Γ-centered Monkhorst-Pack [28] grids for a 24-atom single-layer $CrPS_4$ unit cell, a 24-atom FM bulk $CrPS_4$ unit cell, 24-atom C-type AFM bulk $CrPS_4$ unit cell, and the other three 48-atom AFM bulk $CrPS_4$ supercells, respectively. The lattice parameters of bulk $CrPS_4$, the in-plane lattice constants of single-layer $CrPS_4$, and the atomic positions of all structures are completely relaxed using the conjugate gradient method until the convergence criterion that the residual interatomic forces are below 0.01 eV/Å is satisfied.

To facilitate referencing various magnetic structures, we use notation to denote the arrangement of magnetic moments of Cr atoms. This notation combines the atom labels used in Fig. 1 with an upward or downward arrow in the subscript. The upward and downward arrows symbolize the spin-up and spin-down directions, respectively. The Cr atoms in a neighboring unit cell along the z direction are additionally labeled with a prime symbol in the superscript. With this notation, for example, the A-type AFM ordering is labeled by $I_\uparrow II_\uparrow III_\uparrow IV_\uparrow I'_\downarrow II'_\downarrow III'_\downarrow IV'_\downarrow$. Table I lists all the types of magnetic structures considered in this work and their corresponding notations.

We adopt the finite-displacement method [29] as implemented in PHONOPY [30] to calculate the phonon spectrum of single-layer $CrPS_4$. The symmetry of single-layer $CrPS_4$ results in thirty-six $3 \times 3 \times 1$ supercells with inequivalent atomic displacements. For the force calculations with VASP, only the Γ point of each supercell is used.

III. RESULTS AND DISCUSSION

We first examine whether the above simulation parameters are able to reproduce several basic properties of bulk $CrPS_4$, including lattice parameters, ground-state magnetic structure, and electronic band gap, all of which have corresponding

TABLE I. Lattice parameters a (Å), b (Å), c (Å), and β (degrees); energy difference ΔE (meV per formula unit); band gap (eV); and electron magnetic moment m (in units of μ_B) per Cr atom of bulk $CrPS_4$ calculated with the PBE and vdW-DF-optB88 functionals. The energy difference is computed using the energy of the A-type AFM structure as the reference.

Magnetic ordering	Method	a	b	c	β	ΔE	E_g	m
FM	PBE	10.88	7.33	6.89	91.64	0.25	1.10,[a] 1.35[b]	2.58
$I_\uparrow II_\uparrow III_\uparrow IV_\uparrow I'_\uparrow II'_\uparrow III'_\uparrow IV'_\uparrow$	vdW-DF-optB88	10.93	7.27	6.09	92.23	1.19	1.01,[a] 1.17[b]	2.58
A-type AFM	PBE	10.88	7.33	6.88	91.60	0	0.79	2.58
$I_\uparrow II_\uparrow III_\uparrow IV_\uparrow I'_\downarrow II'_\downarrow III'_\downarrow IV'_\downarrow$	vdW-DF-optB88	10.93	7.27	6.09	92.21	0	0.73	2.58
C-type AFM	PBE	10.93	7.24	6.88	91.25	19.35	1.32	2.51
$I_\uparrow II_\downarrow III_\uparrow IV_\downarrow I'_\uparrow II'_\downarrow III'_\uparrow IV'_\downarrow$	vdW-DF-optB88	10.98	7.19	6.11	91.80	10.40	1.23	2.51
E-type AFM	PBE	10.91	7.28	6.87	91.46	13.50	1.02	2.54
$I_\uparrow II_\uparrow III_\downarrow IV_\uparrow I'_\downarrow II'_\downarrow III'_\uparrow IV'_\downarrow$	vdW-DF-optB88	10.95	7.23	6.10	91.99	8.71	0.96	2.54
G-type AFM	PBE	10.94	7.24	6.89	91.22	19.07	1.28	2.51
$I_\uparrow II_\downarrow III_\uparrow IV_\downarrow I'_\downarrow II'_\uparrow III'_\downarrow IV'_\uparrow$	vdW-DF-optB88	10.98	7.19	6.11	91.79	11.23	1.16	2.51
NM	PBE	11.45	6.52	6.88	89.89	781.37	0[c]	
	vdW-DF-optB88	11.45	6.59	6.17	89.05	671.27	0[c]	
Undetermined	Experiment [15]	10.87	7.25	6.14	91.88			
AFM	Experiment [16]	10.86	7.25	6.14	91.87		1.40	
AFM	Experiment [17]	10.86	7.25	6.14	91.88		0.17	

[a]Spin up.
[b]Spin down.
[c]Metallic.

experimental data for comparison. Bulk $CrPS_4$ crystallizes as a monoclinic structure with the $C2$ space group [16]; it therefore has four independent lattice parameters: a, b, c, and angle β. Table I reports the calculated lattice parameters using both the PBE and vdW-DF-optB88 functionals. For the completeness of comparison, we also list the results of the nonmagnetic (NM) structure, for which no spin-polarized DFT calculations are involved. As can be seen from Table I, the resulting lattice parameters are nearly independent of the FM and AFM structures. We also observe that, although the PBE functional leads to a, b, and β that agree well with the experimental data, the lattice constant c seems to be overestimated. Including the vdW-DF-optB88 functional is thus important to obtain excellent agreement between the theoretical and experimental lattice constant c. The lattice parameters a, b, and β of the NM structure, on the other hand, are quite different from all of the FM, AFM, and experimental results.

We next compare the total energies of FM and four AFM bulk $CrPS_4$ structures. Table I reveals the ground-state magnetic structure of bulk $CrPS_4$ exhibits the A-type AFM ordering because the energy differences between the other magnetic structures and the A-type AFM structure are all positive. We also notice that the total energy of the FM structure is nearly identical to that of the A-type AFM structure, and the NM structure shows much larger energy differences than the other structures. The predicted AFM ordering is, overall, consistent with the two above-mentioned experiments which measured the temperature-dependent magnetic susceptibility [16,17]. However, our predicted AFM type is different from the C type suggested in Ref. [17]. Table I contrastingly shows the energy of C-type AFM structure is higher than that of the A-type AFM structure. Determination of the type of AFM ordering requires the neutron diffraction technique. Future experiments involving this technique are therefore called for to provide decisive evidence of the type of AFM ordering in bulk $CrPS_4$. Given that the A-type AFM ordering exhibits the minimum total energy, we therefore use it as the reference to calculate the formation energy of single-layer bulk $CrPS_4$ (see below).

Figure 2 shows the density of states (DOS) of FM, AFM, and NM bulk $CrPS_4$ computed with the PBE and vdW-DF-optB88 functionals. All the magnetic structures except the NM one are semiconducting. Table I summarizes the theoretical band gaps and available experimental data. The optical transmission spectra reported in Ref. [16] show that bulk $CrPS_4$ is an indirect band gap semiconductor with a band gap of around 1.40 eV. The band gap (0.79 eV) of A-type AFM bulk $CrPS_4$ calculated with the PBE functional is expectedly smaller than the experimental band gap since the PBE functional underestimates the band gap due to self-interaction errors [31–33]. Interestingly, Ref. [17] reports a drastically smaller band gap (0.17 eV). In this reference, instead of measuring the optical spectra, the band gap is derived from the variation of electrical resistivity with temperature via the relation $\rho \propto Eg/k_BT$. While this temperature dependence of the resistivity is true for an intrinsic semiconductor, a semiconductor is often an extrinsic one with a dominant (n or p) type of impurity. Therefore, the reported band gap in Ref. [17] most likely corresponds to the donor or acceptor ionization energy, as a similar exponential relation

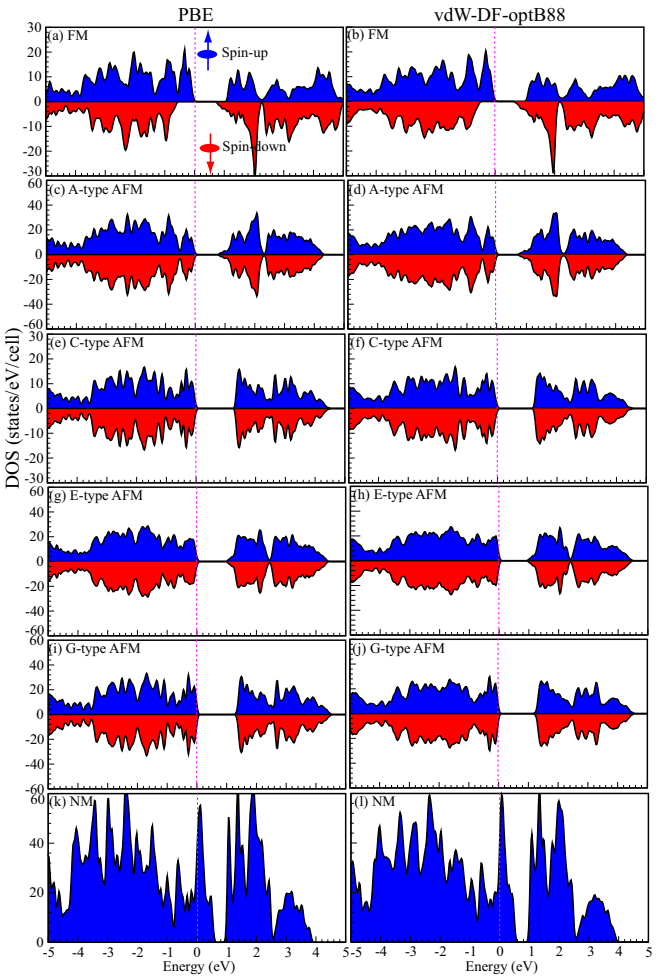

FIG. 2. DOS of bulk $CrPS_4$ with (a) and (b) FM, (c)–(j) four different types of AFM, and (k) and (l) NM structures obtained from DFT calculations with the PBE and vdW-DF-optB88 functionals.

exists between the resistivity, ionization energy, and temperature [34].

A-type AFM bulk $CrPS_4$ exhibits FM ordering within each layer but AFM ordering between layers. We therefore expect the magnetic structure of single-layer $CrPS_4$ to become FM as the number of layers is reduced to one. Indeed, our PBE energy calculations show that single-layer $CrPS_4$ with FM ordering ($I_\uparrow II_\uparrow III_\uparrow IV_\uparrow$) is more stable than other possible magnetic structures. For example, the PBE total energies of the $I_\uparrow II_\uparrow III_\downarrow IV_\downarrow$ and $I_\uparrow II_\downarrow III_\downarrow IV_\uparrow$ structures are, respectively, 4.56 and 27.07 meV/f.u. higher than that of the FM structure. The occurrence of FM ordering in single-layer $CrPS_4$ appears to contradict the remarkable Mermin-Wagner theorem claiming the absence of long-range order in a two-dimensional (2D) system [35]. However, noncollinear calculation including spin-orbit coupling shows single-layer $CrPS_4$ exhibits a sizable anisotropy energy of 40.0 μeV per Cr atom with the spins favorably aligned along the out-of-plane (z) direction. This magnetocrystalline anisotropy implies single-layer $CrPS_4$ belongs to the category of 2D Ising magnets, which are a notable exception of the Mermin-Wagner theorem [36].

TABLE II. In-plane lattice constants a and b (Å) and electron magnetic moment m (in units of μ_B, the Bohr magneton) per Cr atom and formation energy E_f^{PBE} (meV/atom) of single-layer $CrPS_4$ calculated with the DFT-PBE method. The formation energy E_f^{vdW} calculated with the vdW-DF-optB88 functional is also shown for comparison.

a	b	m	E_f^{PBE}	E_f^{vdW}
10.86	7.32	2.58	1.44	71.60

Table II lists the in-plane lattice constants (a and b) of single-layer $CrPS_4$ and the electron magnetic moment of each Cr atom. These parameters are very similar to the values they are in bulk $CrPS_4$. The optimized Cr_I-Cr_{IV} and Cr_{II}-Cr_{III} distances are both 5.43 Å, which is much longer than the Cr_I-Cr_{II} and Cr_{III}-Cr_{IV} distances, which are 3.73 and 3.59 Å, respectively.

We proceed to evaluate the stability of single-layer $CrPS_4$. First, we adopt the common definition of the formation energy ΔE_f for a 2D material; that is, the ΔE_f of single-layer $CrPS_4$ is calculated via subtracting the energy of single-layer FM $CrPS_4$ from A-type AFM bulk $CrPS_4$ [37]. Table II shows that the ΔE_f of single-layer $CrPS_4$ are 1.44 and 71.60 meV/atom calculated for the PBE and vdW-DF-optB88 functionals, respectively. These formation energies are sufficiently small, indicating that one feasible way of fabricating single-layer $CrPS_4$ sheets is mechanically exfoliating synthesized bulk $CrPS_4$. Second, we assess the dynamical stability of single-layer $CrPS_4$. Figure 3 shows the calculated phonon spectrum of single-layer $CrPS_4$. The absence of imaginary phonon modes confirms the dynamical stability.

Having established the ground-state magnetic structure of single-layer $CrPS_4$, we set out to understand the electronic origin that gives rise to FM ordering in the 2D structure. We notice that the electron magnetic moment of each Cr atom in bulk (Table I) and single-layer $CrPS_4$ (Table II) is close to $3.0\mu_B$, resulting from the oxidation state of +3 in a Cr ion. The strongly localized magnetic moment suggests invoking exchange models to understand the mechanism of ferromagnetism. Along the y direction, the distance between Cr atoms is too large for the direct-exchange coupling to play an important role. The optimized Cr_{III}-S_V-Cr_V angle is 95.7°, which is near the ideal 90° bond angle usually associated with FM ordering, according to the Goodenough-Kanamori rules [38–40]. We therefore understand the exchange interactions between the Cr atoms through the superexchange interactions along the y direction. The exchange interactions along the x direction are more indirect because the Cr-Cr distance is even larger. This indirect exchange coupling is not only mediated by S atoms but also by P atoms, each of which is fourfold coordinated to surrounding S atoms. Figure 4 illustrates the total charge-density difference between the $I_\uparrow II_\uparrow III_\uparrow IV_\uparrow$ (FM) and $I_\uparrow II_\uparrow III_\downarrow IV_\downarrow$ (AFM) magnetic structures. We observe significant charge redistributions around Cr and S atoms, implying strong exchange coupling along the x direction, which is also reflected by the above-shown sizable energy difference between the two magnetic structures.

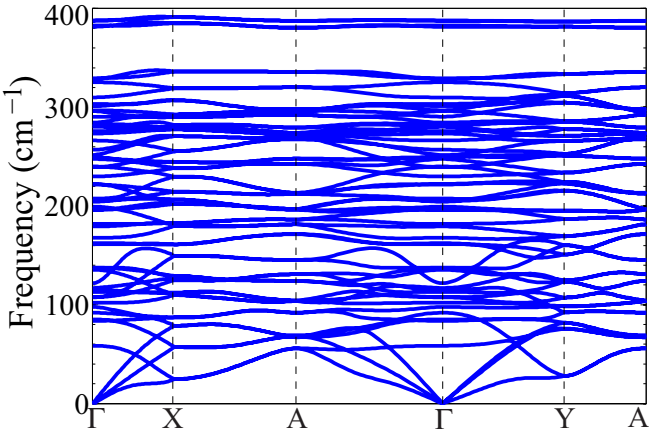

FIG. 3. Theoretical phonon spectrum of single-layer $CrPS_4$ obtained from DFT calculations with the PBE functional. The high-symmetry q points Γ, X, A, and Y have fractional coordinates of (0, 0), (1/2, 0), (1/2, 1/2), and (0, 1/2) of the 2D reciprocal lattice vectors, respectively.

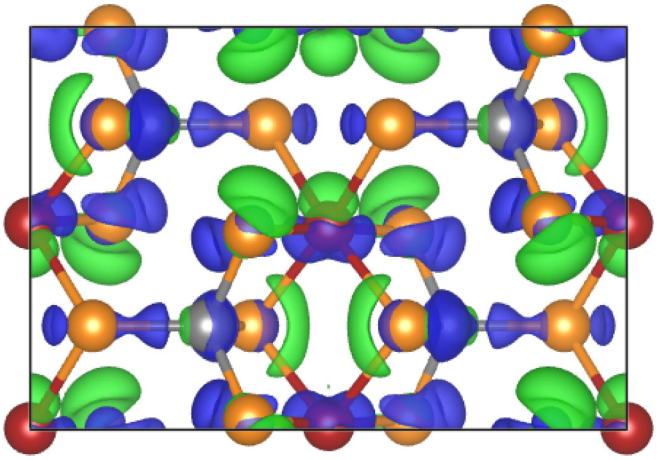

FIG. 4. Charge-density difference between FM and AFM single-layer $CrPS_4$. Green and blue refer to electron accumulation and depletion, respectively. The isosurface value is set to 0.001 e/a_0^3, with a_0 being the Bohr radius.

Figure 5 displays the PBE band structures of the spin-up and spin-down electrons. The spin-up band structure exhibits an indirect band gap of 1.13 eV with the conduction band minimum (CBM) located at the Γ point and the valence band maximum (VBM) at the A point. The CBM is twofold degenerate, with the effective masses of the heavy and light electrons being $1.96\,m_0$ and $1.26\,m_0$, respectively, where m_0 is the rest mass of the electron. The hole effective mass m_h at the VBM is $0.76\,m_0$, which is significantly smaller and only slightly heavier than that of single-layer MoS_2 with a theoretical m_h of $0.54\,m_0$ [41]. By contrast, the band gap of 1.42 eV in the spin-down band structure is direct and wider than that of the spin-up band gap. The electron and hole effective masses are $0.87\,m_0$ and $1.52\,m_0$, respectively. Both spin-up and spin-down band gaps are significantly larger than the band gap of A-type AFM bulk $CrPS_4$ due to the quantum confinement effect. Owing to the much smaller hole effective

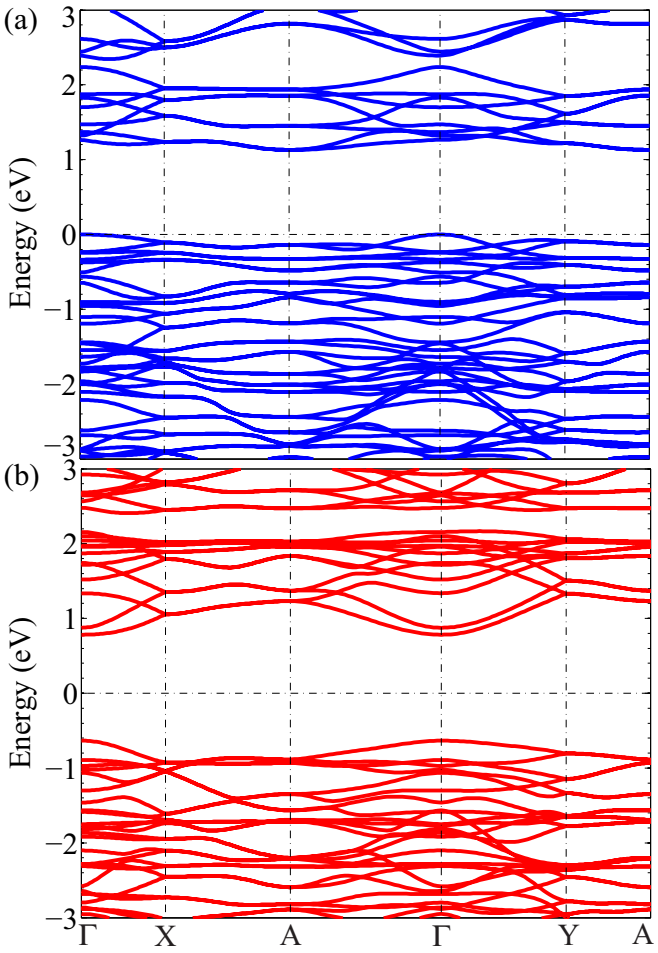

FIG. 5. (a) Spin-up and (b) spin-down band structures of single-layer $CrPS_4$ calculated with the DFT-PBE method. The Fermi level of the spin-up band structure is set to zero, while the spin-down band structure is shifted by the same magnitude of electron energy.

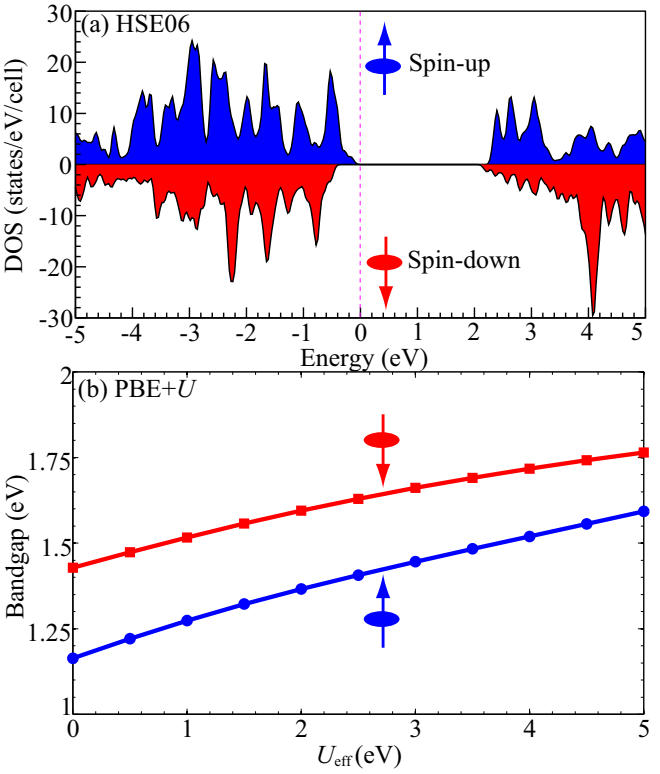

FIG. 6. (a) DOS of single-layer bulk $CrPS_4$ calculated with the DFT-HSE06 method. (b) Variation of spin-up and spin-down band gaps with the U_{eff} parameters.

mass, we suggest p-type doping is an effective strategy to attain the highest carrier mobility when using single-layer $CrPS_4$ in electronic devices.

We also employ the Heyd-Scuseria-Ernzerhof [42,43] (HSE06) hybrid density functional to obtain more accurate band gaps of single-layer $CrPS_4$. Figure 6(a) shows the resulting HSE06 spin-up and spin-down DOSs, with corresponding band gaps of 2.42 and 2.61 eV, respectively. These band gaps are within the visible-light spectrum, suggesting that single-layer $CrPS_4$ is a promising candidate for a variety of solar-energy-conversion applications. In addition to using the HSE06 functional, we attempt to calculate the band gaps of single-layer $CrPS_4$ using a computationally cheaper PBE + U method with the rotationally invariant U_{eff} [44]. We vary the U_{eff} parameters from 0 to 5.0 eV. Figure 6(b) shows the U_{eff}-dependent spin-up and spin-down band gaps. Both the spin-up and spin-down band gaps increase nearly linearly with the U_{eff} parameters. The two curves in Fig. 6(b) are almost parallel to each other, showing that the difference between the two gaps is independent of the U_{eff} parameter. The average increasing rate of the two band gaps is about 0.06; that is, adding 1.0 eV to the U_{eff} only increases the band gaps by around 0.06 eV. As a result, if the HSE06 band gaps are used as the references and we assume a constant increasing rate of the band gaps with U_{eff}, an unphysically large U_{eff} parameter must be used in order to obtain the same magnitudes of the HSE06 band gaps.

Since single-layer $CrPS_4$ exhibits band gaps that are within the visible-light spectrum, we demonstrate an example of a potential solar-energy-conversion application of single-layer $CrPS_4$ as a photocatalyst for water splitting. Note that magnetism is not necessary for water splitting. However, we shall see that magnetism leads to spin-dependent optical properties. In the context of water splitting, two parameters, the optical absorption and band-edge positions, are of main relevance. For sunlight polarized within the plane of single-layer material $CrPS_4$, the optical absorbance $A(\omega)$ is calculated as $A(\omega) = \omega/cL\epsilon_{xx/yy}$ [45,46], where c is the speed of light in vacuum and L is the length of the supercell in the z direction. The random-phase approximation and the PBE functional are adopted to calculate the xx and yy components of the imaginary part of the dielectric constant tensor [47]. Figure 7 shows that the optical absorbance strongly depends not only on the polarization vectors of the light but also on the spin directions. The first absorption peaks in the optical absorption spectra originate from the excitations of the spin-up electrons. This is because the top valence band and the bottom conduction band in the spin-up band structure (Fig. 5) are almost parallel at most k points in the first Brillouin zone, which lead to a significantly enhanced joint density of states and the absorption peaks. The total optical absorbance of single-layer $CrPS_4$

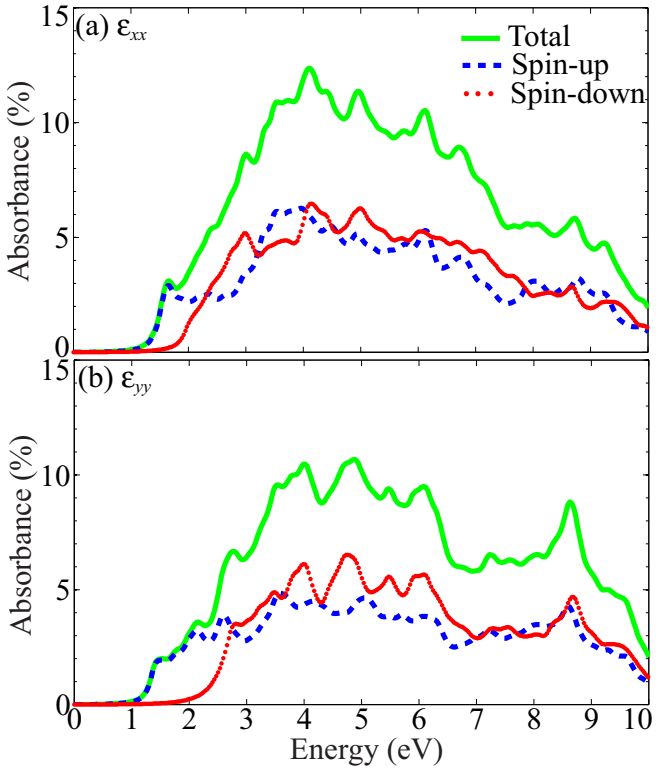

FIG. 7. Optical absorbance of single-layer $CrPS_4$ transformed from the (a) xx and (b) yy components of the imaginary part of the dielectric constant tensor calculated at the DFT PBE level of theory.

around the first peaks ranges from 2% to 3%, which is similar to that (2.3%) of single-layer graphene [48].

To determine the band-edge positions of single-layer $CrPS_4$ with reference to the redox potentials of water splitting at pH = 0, we adopt Toroker's method [49] to calculate the energy level of the band gap center (BGC) E_{BGC} of single-layer $CrPS_4$ with the assumption that the E_{BGC} is independent of the functionals used. The conduction and valence band edges are $E_{BGC} + E_g/2$ and $E_{BGC} - E_g/2$, respectively. This method has been used to calculate the band-edge positions of a number of single-layer semiconductors [50,51] such as group-III monochalcogenides [52]. Figure 8 illustrates the potential profiles and the corresponding spin-up and spin-down E_{BGC} determined as −5.15 and −5.65 eV, respectively. The exchange-correlation potential is not included in the potential profiles, which are therefore spin independent. We use the HSE06 band gaps to evaluate the band-edge energy positions; then the conduction and valence band-edge energy levels for the spin-up electrons are −3.94 and −6.36 eV, respectively. Similarly, the conduction and valence band-edge energy levels for the spin-down electrons are −4.34 and −6.95 eV, respectively. The standard redox potentials (−4.44 and −5.67 eV) of the water-splitting reaction lie between

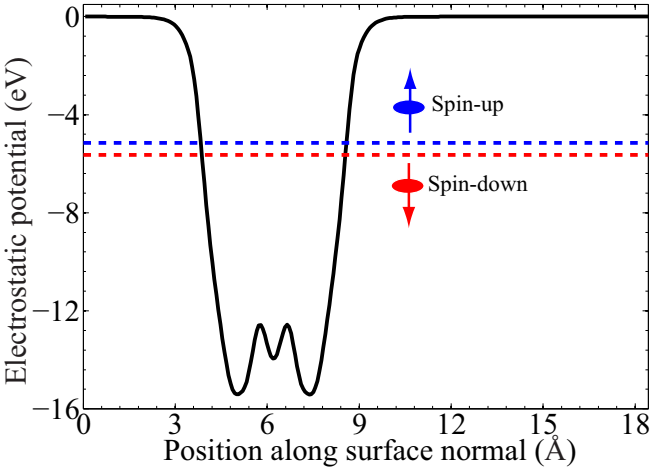

FIG. 8. Electrostatic potential profiles and E_{BGC} of single-layer $CrPS_4$ calculated with the DFT-PBE method. The vacuum energy level is set to zero.

the calculated band-edge energy levels for both spin-up and spin-down electrons. We therefore suggest single-layer $CrPS_4$ could be a suitable photocatalyst for solar water splitting.

IV. CONCLUSIONS

In summary, we performed DFT calculations to show that the ground-state magnetic structure of bulk $CrPS_4$ is AFM, which is consistent with the experiment. We also found that the type of AFM ordering should be the A type. This prediction awaits experimental confirmation using the neutron diffraction technique. We further predicted that single-layer $CrPS_4$ remains to be a semiconductor with enlarged spin-up and spin-down band gaps. However, the magnetic structure transforms to FM ordering due to the dimension reduction to an ultrathin layer. Finally, we showed a potential application of single-layer $CrPS_4$ as a photocatalyst for splitting water to generate hydrogen gas. We expect this work to stimulate interest in realizing single-layer $CrPS_4$ sheets in experiment. Future theoretical work includes studies of the magnetism effects on the other properties (e.g., thermoelectric and piezoelectric) of semiconducting single-layer $CrPS_4$.

ACKNOWLEDGMENTS

This research is supported by the National Natural Science Foundation of China (Grant No. 51602079) and the Fundamental Research Funds for the Central Universities of China (Grant No. AUGA5710013115). This work used computational resources of the National Supercomputing Center of China in Shenzhen (Shenzhen Cloud Computing Center) and the Texas Advanced Computing Center under Contract No. TG-DMR-140067. We thank Prof. R. G. Hennig for helpful discussions.

[1] I. G. Austin and D. Elwell, Contemp. Phys. **11**, 455 (1970).
[2] W. L. Roth, Phys. Rev. **110**, 1333 (1958).
[3] G. A. Sawatzky and J. W. Allen, Phys. Rev. Lett. **53**, 2339 (1984).

[4] L. Goldstein, D. H. Lyons, and P. Gibart, Solid State Commun. **13**, 1503 (1973).
[5] T. J. Williams, A. A. Aczel, M. D. Lumsden, S. E. Nagler, M. B. Stone, J.-Q. Yan, and D. Mandrus, Phys. Rev. B **92**, 144404 (2015).
[6] X. Li and J. Yang, J. Mater. Chem. C **2**, 7071 (2014).
[7] H. L. Zhuang, Y. Xie, P. R. C. Kent, and P. Ganesh, Phys. Rev. B **92**, 035407 (2015).
[8] N. Sivadas, M. W. Daniels, R. H. Swendsen, S. Okamoto, and D. Xiao, Phys. Rev. B **91**, 235425 (2015).
[9] J. He, P. Lyu, L. Z. Sun, A. Morales Garcia, and P. Nachtigall, J. Mater. Chem. C **4**, 6500 (2016).
[10] M. Kan, J. Zhou, Q. Sun, Y. Kawazoe, and P. Jena, J. Phys. Chem. Lett. **4**, 3382 (2013).
[11] M. Kan, S. Adhikari, and Q. Sun, Phys. Chem. Chem. Phys. **16**, 4990 (2014).
[12] H. L. Zhuang and R. G. Hennig, Phys. Rev. B **93**, 054429 (2016).
[13] E. B. Isaacs and C. A. Marianetti, Phys. Rev. B **94**, 035120 (2016).
[14] X. Zhang, X. Zhao, D. Wu, Y. Jing, and Z. Zhou, Adv. Sci. **3**, 1600062 (2016).
[15] R. Diehl and C.-D. Carpentier, Acta Crystallogr., Sect. B **33**, 1399 (1977).
[16] A. Louisy, G. Ouvrard, D. Schleich, and R. Brec, Solid State Commun. **28**, 61 (1978).
[17] Q. L. Pei, X. Luo, G. T. Lin, J. Y. Song, L. Hu, Y. M. Zou, L. Yu, W. Tong, W. H. Song, W. J. Lu, and Y. P. Sun, J. Appl. Phys. **119**, 043902 (2016).
[18] G. Kresse and J. Furthmüller, Phys. Rev. B **54**, 11169 (1996).
[19] G. Kresse and J. Hafner, Phys. Rev. B **47**, 558 (1993).
[20] J. P. Perdew, K. Burke, and M. Ernzerhof, Phys. Rev. Lett. **77**, 3865 (1996).
[21] M. Dion, H. Rydberg, E. Schröder, D. C. Langreth, and B. I. Lundqvist, Phys. Rev. Lett. **92**, 246401 (2004).
[22] G. Román-Pérez and J. M. Soler, Phys. Rev. Lett. **103**, 096102 (2009).
[23] T. Thonhauser, V. R. Cooper, S. Li, A. Puzder, P. Hyldgaard, and D. C. Langreth, Phys. Rev. B **76**, 125112 (2007).
[24] J. Klimeš, D. R. Bowler, and A. Michaelides, J. Phys. Condens. Matter **22**, 022201 (2010).
[25] G. Kresse and D. Joubert, Phys. Rev. B **59**, 1758 (1999).
[26] P. E. Blöchl, Phys. Rev. B **50**, 17953 (1994).
[27] G. Bergerhoff and I. D. Brown, in *Crystallographic Databases* (International Union of Crystallography, Chester, UK, 1987) .
[28] H. J. Monkhorst and J. D. Pack, Phys. Rev. B **13**, 5188 (1976).
[29] L. Chaput, A. Togo, I. Tanaka, and G. Hug, Phys. Rev. B **84**, 094302 (2011).
[30] A. Togo and I. Tanaka, Scr. Mater. **108**, 1 (2015).
[31] J. P. Perdew and M. Levy, Phys. Rev. Lett. **51**, 1884 (1983).
[32] L. J. Sham and M. Schlüter, Phys. Rev. Lett. **51**, 1888 (1983).
[33] P. Mori-Sánchez, A. J. Cohen, and W. Yang, Phys. Rev. Lett. **100**, 146401 (2008).
[34] J. S. Blakemore, *Semiconductor Statistics* (Dover, New York, 1987).
[35] N. D. Mermin and H. Wagner, Phys. Rev. Lett. **17**, 1133 (1966).
[36] S. Blundell, *Magnetism in Condensed Matter* (Oxford University Press, Oxford, 2001).
[37] H. L. Zhuang and R. G. Hennig, JOM **66**, 366 (2014).
[38] J. B. Goodenough, Phys. Rev. **100**, 564 (1955).
[39] J. B. Goodenough, J. Phys. Chem. Solids **6**, 287 (1958).
[40] J. Kanamori, J. Phys. Chem. Solids **10**, 87 (1959).
[41] A. Ramasubramaniam, Phys. Rev. B **86**, 115409 (2012).
[42] J. Heyd, G. E. Scuseria, and M. Ernzerhof, J. Chem. Phys. **118**, 8207 (2003).
[43] J. Heyd, G. E. Scuseria, and M. Ernzerhof, J. Chem. Phys. **124**, 219906 (2006).
[44] S. L. Dudarev, G. A. Botton, S. Y. Savrasov, C. J. Humphreys, and A. P. Sutton, Phys. Rev. B **57**, 1505 (1998).
[45] L. Yang, J. Deslippe, C.-H. Park, M. L. Cohen, and S. G. Louie, Phys. Rev. Lett. **103**, 186802 (2009).
[46] M. Bernardi, M. Palummo, and J. C. Grossman, Nano Lett. **13**, 3664 (2013).
[47] M. Gajdoš, K. Hummer, G. Kresse, J. Furthmüller, and F. Bechstedt, Phys. Rev. B **73**, 045112 (2006).
[48] R. R. Nair, P. Blake, A. N. Grigorenko, K. S. Novoselov, T. J. Booth, T. Stauber, N. M. R. Peres, and A. K. Geim, Science **320**, 1308 (2008).
[49] M. C. Toroker, D. K. Kanan, N. Alidoust, L. Y. Isseroff, P. Liao, and E. A. Carter, Phys. Chem. Chem. Phys. **13**, 16644 (2011).
[50] J. Liu, X.-B. Li, D. Wang, W.-M. Lau, P. Peng, and L.-M. Liu, J. Chem. Phys. **140**, 054707 (2014).
[51] A. K. Singh, K. Mathew, H. L. Zhuang, and R. G. Hennig, J. Phys. Chem. Lett. **6**, 1087 (2015).
[52] H. L. Zhuang and R. G. Hennig, Chem. Mater. **25**, 3232 (2013).